Boron nitride-based nano-biocomposites: Design by 3D printing for bone tissue engineering

Habib Belaid, Sakthivel Nagarajan, Carole Barou, Vincent Huon, Jonathan Barés, Sebastien Balme, Philippe Miele, David Cornu, Vincent Cavaillès, Catherine Teyssier, et al.

Boron nitride-based nano-biocomposites: Design by 3D printing for bone tissue engineering

*Habib Belaid[1,2], Sakthivel Nagarajan[1], Carole Barou[1,2,3], Vincent Huon[4], Jonathan Bares[4], Sébastien Balme[1], Philippe Miele[1], David Cornu[1], Vincent Cavaillès,[2] Catherine Teyssier[2] and Mikhael Bechelany[1]**

[1]Institut Européen des Membranes, UMR 5635 Université Montpellier, CNRS, ENSCM, Place Eugene Bataillon, F-34095 Montpellier cedex 5, France

[2]IRCM, Institut de Recherche en Cancérologie de Montpellier, INSERM U1194, Université Montpellier, Montpellier F-34298, France

[3]Biologics 4 life, 84120 Pertuis, France

[4]LMGC, Laboratoire de Mécanique et Génie Civil, Université Montpellier, CNRS, Montpellier, France

* Corresponding author:

mikhael.bechelany@umontpellier.fr, Phone: +33467149167, Fax: +33467149119

Keywords: polylactic acid, boron nitride, bionanocomposite, 3D printing, tissue engineering

ABSTRACT

The aim of this work was to develop a bioresorbable, biodegradable and biocompatible synthetic polymer with adequate mechanical properties for bone tissue engineering applications. Polylactic acid (PLA) biomimetic biodegradable scaffolds, generated by 3D printing using the fused deposition modeling method, were reinforced by incorporation of exfoliated boron nitride (EBN). The physicochemical analysis by X-ray diffraction and Raman spectroscopy confirmed the filler presence. Thermogravimetric analysis and differential scanning calorimetry showed that EBN incorporation did not modify the transition temperature, but decreased the polymer crystallinity. Morphology analysis by scanning electron microscopy indicated that the scaffolds had an average pore size of 500 μm. A tensile test demonstrated that the mechanical properties were not affected following EBN incorporation. Conversely, the surface roughness was modified upon EBN addition. Moreover, contact angle measurements showed a transition from a hydrophobic surface for the pure PLA to a hydrophilic surface for the PLA/EBN scaffold. Finally, the results of cytotoxicity, cell attachment and proliferation assays using MG-63 and MC3T3 cells indicated that PLA/EBN scaffolds are non-toxic and cytocompatible. Furthermore, EBN addition promoted MG-63 cell mineralization on the PLA scaffold. In conclusion, this new 3D printed nanocomposite appears as a promising scaffold for tissue engineering.

1. INTRODUCTION.

For decades, bone disorder management has been a challenge due to the limited self-repair after critical damage[1]. Therefore, passive artificial junctions are often implanted surgically[2]. However, their removal after recovery is recommended, and this requires additional surgery. Regenerative tissue engineering allows overcoming the lack of bioactivity of passive implants. Scaffold-assisted regeneration methods are one of the most advantageous regenerative tissue engineering techniques. To facilitate cell adhesion and proliferation, it is crucial that the physico-chemical properties mimic the multi-scale structure of the bone extracellular matrix[3,4]. Indeed, the scaffold has to possess an interconnected porous network with a pore size and morphology that allows cells migration[5]. Moreover the chemical composition and the mechanical properties of the scaffolds could influence the regeneration of the tissue[6,7].

Biomimetic bone scaffolds are fabricated using biodegradable polymers, such as gelatin[8], polycaprolactone[9] and polylactic acid (PLA)[10]. PLA is a well-known and popular polymer synthesized from bio-sourced materials, such as corn and cellulose[11], and currently the only one produced worldwide. [12] It is widely used for biomedical applications, such as sutures[13] and orthopedic fixation[14].

Unfortunately, such biodegradable synthetic materials usually have surface state properties that are incompatible with biological tissues[15]. These properties could be improved by integrating boron nitride (BN), in its graphene form, in the scaffold formulation[16]. BN is an isoelectric analogue of graphite, non-toxic to cells, and BN-functionalized polymers are highly dispersed in aqueous and organic solvents[17]. Among the different nanofillers to reinforce polymer matrices, BN is electrically insulated and has major chemical, mechanical and thermal stability[18]. Moreover, BN nanosheet synthesis does not involve the use of acids or organic solvents[19]. BN use in biomedical fields has been much studied[20]. For example, our

laboratory successfully exfoliated BN using gelatin and fabricated electrospun gelatin fibers reinforced with BN to improve their mechanical properties without affecting cell viability and proliferation[21]. Other studies have shown that BN nanotubes have a good potential for biomedical applications[17,22]. Moreover, boron-containing compounds are interesting for anticancer therapy[23], particularly in material composites for drug loading and release[24]. Moreover, BN nanotubes improve cell differentiation *in vitro*[25] and *in vivo*[26].

In tissue engineering, many different methods have been used for scaffold fabrication, such as solvent casting/particulate leaching[27], emulsion freeze drying[28], phase separation[29] and electrospinning[30]. However, these techniques are limited by the poor control of pore size and 3D architecture, and by the difficulty to process into different shapes. On the other hand, 3D printing allows printing customized structures (size, geometry, porosity) for tissue repair and regeneration[31,32]. 3D printing techniques, such as stereolithography[33], 3D plotting[34], selective laser sintering[35], bioprinting[36] and fused deposition modeling (FDM)[37], are employed to print various polymers and polymer composites. Different studies have demonstrated that the 3D controlled architecture of the scaffold significantly affects its mechanical properties[38,39] as well as cell adhesion and proliferation[40,41]. Therefore, 3D printing can be used to put in shape BN-based nanocomposites in order to obtain a final material with improved mechanical properties. For example, FDM has been used to print different BN-based polymers, such as thermoplastic polyurethane or acrylonitrile-butadiene-styrene, with better thermal conductivity[42,43], while a photosensitive BN nanoplatelet-based polymer printed using stereolithography showed enhanced damping behavior[44]. A bio-ink containing poly-lactic-co-glycolic acid (PLGA)-based hexagonal BN was used to print a nanomaterial for bioelectronic applications. This study showed that the mechanical and thermal properties could be controlled using the right amount of filler without inducing any cytotoxicity[45]. However, to

the best of our knowledge, no study tried to improve BN capacity to enhance the bioactivity properties of 3D printed polymer materials for bone tissue engineering.

Therefore, the objective of this work was to create a 3D porous scaffold with controlled architecture and adequate composition to support bone cell adhesion. Using FDM, a 3D multifunctional PLA composite scaffold was fabricated with an interconnected porous structure and reinforced with exfoliated BN (PLA/EBN). Different parameters were analyzed to assess the influence of BN addition to PLA on the adhesion, proliferation and differentiation of osteosarcoma cells. Our results suggested that this new PLA/EBN scaffold is a very interesting support for a potential use in bone regeneration.

2. EXPERIMENTAL SECTION.

2.1. Materials. PLA pellets were purchased from Natureworks LLC. Type A gelatin (48722-500G-F) obtained from porcine skin (gel strength 170−195 g Bloom, CAS 9000-70-8), dichloromethane (CH_2Cl_2, <99.9%, CAS 75-09-2), ethanol (96% vol, CAS 64-17-5), 37% formaldehyde (FA, 37 wt. % in H_2O, CAS 50-00-0), 25% glutaraldehyde (GTA, 25% in H_2O, CAS 111-30-8), cetylpyridinium chloride (CAS 6004-24-6), phosphate-buffered saline (PBS) (P44717) tablets, Triton X 100 (CAS 9002-93-11), bovine serum albumin (BSA) (≥98%, CAS 9048-46-8), Mowiol 40-88 (CAS 9002-89-5), L-ascorbic acid (CAS 50-81-7), ß-glycerophosphate (≥99%, CAS 154804-51-0), Alizarin Red S (CAS 130-22-3), anti-actin antibody (clone CA15, A5441), dexamethasone (≥80%, CAS 50-02-2), Hoechst 33342 (≥98%, CAS 23491-52-3), and 3-(4,5-dimethylthiazol-2-yl)-2,5-diphenyl tetrazolium bromide (MTT, 98%, CAS 298-93-1) were purchased from Sigma-Aldrich. Combat Industrial Boron Nitride powder PHPP325B was purchased from Saint Gobain. Acetone (≥99% (GC), CAS 67-64-1) was purchased from Honeywell. Tween 20 (CAS 9005-64-5) was purchased from VWR International. Alexa-conjugated anti-mouse IgG (Alexa fluor 488, A11001) was purchased from ThermoFisher Scientific. MEM alpha medium (Gibco 12571-063), dimethyl sulfoxide (DMSO) (BDH Prolabo 23486.297), fetal bovine serum (FBS) (Eurobio CVFSVF00-01), penicillin/streptomycin (Gibco 15140-122) and 0.05% trypsin-EDTA (Gibco 25300-054) were used for cell cultures. MG-63 osteosarcoma were from ATCC.and MC3T3-E1 preosteoblast cells were kindly provided by LYOS (Inserm UMR 1033, Lyon, France)

2.2. Preparation of PLA/EBN scaffolds. BN sheets were exfoliated from BN powder as previously described[24]. Briefly, 1 g of BN powder was added to 20% gelatin solution (100 mL) prepared by dissolving gelatin in water at 75°C. To facilitate exfoliation, the solution was sonicated using an ultrasonic probe system (SONOPULS HD 3100) (pulse on/off for 1

second) with 60% amplitude at 50°C overnight. EBN was separated by centrifugation at 6000 rpm for 30 minutes. The resulting precipitates were dried at 80°C for 48 hours and then calcined at 600°C in air for 2 hours to obtain EBN.[25]

The PLA (10 mL of 10% (w/v)) solution was prepared using dichloromethane as solvent.

EBN (0.1wt %) was dispersed in acetone (1 mg per mL) and placed in an ultrasonic bath for 15 minutes. The solution containing EBN was introduced in the polymer solution under constant magnetic stirring until homogeneous. The PLA/EBN dispersion was poured into a Teflon dish and dried at room temperature overnight. The obtained dried polymer was a film that was cut into pieces and introduced into a single screw extruder (Noztek pro) at an extrusion temperature of about 200°C. The nozzle diameter of the extruder (1.75 mm) was suitable for the 3D printer. A filament with a diameter of 1.75 mm was obtained and used for 3D printing with a Prusa Research MK2S 3D printer.

The scaffold was modeled using the computer-aided design (CAD) software (Design Spark Mechanical). Once the scaffold shape was determined, a STL file was created to be analyzed by the Prusa 3D Slicer software. All printing parameters are given in Table S1.

2.3. Chemical and structural properties. Raman spectra of scaffolds and films were obtained in ambient conditions using a HORIBA Jobin Yvon microscope equipped with a 659.55 nm laser. The X-ray diffraction (XRD) patterns of PLA and PLA/EBN scaffolds were recorded using CuKα radiation, 2Θ range of 10-70° with a scan speed of 2°min^{-1}, using the PANalytica Xpert powder XRD system. The Fourier transform infrared (FTIR) spectrum of PLA and PLA/EBN nanocomposites was recorded with a NEXUS instrument, equipped with an attenuated total reflection accessory in the frequency range of 600−4000 cm^{-1}. For FTIR spectrometry, resolution was 4 cm^{-1}, and the signals were averaged from 32 scans.

2.4. Thermal properties. The different scaffolds were analyzed using a DSC 2920 differential scanning calorimeter, equipped with the RCS90 cooling system. Samples were accurately weighed (≈ 4mg) in an aluminum TA pan and sealed. An empty sealed pan was used as a reference. Samples were first cooled to 25°C and then heated up to 210°C with a heating rate of 10°C.min^{-1} using nitrogen as purge gas. The degree of polymer crystallinity was calculated with the following formula: $\chi = \frac{\Delta Hf - \Delta Hcf}{\Delta H\infty}$ where ΔHf is the enthalpy of fusion, ΔHcf is the enthalpy of cold crystallization, and $\Delta H\infty$ is the reference melting enthalpy for 100% crystalline polymer (ΔH_{∞}= 93 J.g^{-1}).

The resulting differential scanning calorimetry (DSC) curves were analyzed to determine the polymer glass transition (T_g) temperature, melting temperature (Tm), cold crystallization temperature (Tcc), and crystallinity (X_C). The thermogravimetric analysis (TGA) was performed with a TGA G500 apparatus (TA Instruments). About 10mg of each sample was heated from room temperature to 900°C in air atmosphere at a heating rate of 10°C min^{-1}.

2.5. Mechanical properties. The mechanical properties of the 3D printed PLA/EBN scaffold were characterized with standard centimeter samples loaded using a MTS (1/ME) traction machine coupled with a 5 kN force sensor. Samples were printed in the shape of a dog bone (40 mm length, 4 mm width, and 1.5 mm thick) (Figure S1), clamped between jaws, and pulled at a constant speed of 0.01 mm s^{-1} until they broke. During loading, samples were imaged with a 16 Mb camera (SVS-VISTEK) at 1 Hz. Initially, samples were randomly patterned with thin black paint to perform digital image correlation (DIC). Using a DIC algorithm dedicated to large deformations and already presented[46,47], the sample strain changes were reliably computed without inaccuracy coming from the machine and the jaws. Linear elastic regions from the stress−strain graphs were used to calculate the Young's

modulus from at least three trials. The stress at which samples began to break was also measured.

2.6. Morphological properties. The size, morphology, and microstructure of the scaffolds were analyzed using a HITACHI S4800 scanning electron microscopy (SEM) system. For this, scaffolds were coated with platinum using a Polaron SC7620 Mini Sputter Coater. The Image J software was used to calculate the diameter of the struts and of the obtained pores. A stylus profilometer STIL equipped with a CHR1000 captor was used to characterize the 3D topography of 10mm cylinder surface areas of 3D printed PLA and PLA/EBN scaffolds. Determinations were made on two different locations of 2*2 mm for each scaffold with 5 µm step. The SurfaceMap software was used for data post-treatment. The chosen area roughness parameter was Sa (i.e., the surface arithmetical mean height).

A B-CAM-21-BW (CCCIR) monochrome camera and a Led R60 lamp (Conrad) were used to measure the contact angles of ultrapure water on 3D printed PLA and PLA/EBN scaffolds by the sessile drop method[48]. Equilibrium contact angles (considered at 60 seconds) were measured for 5 µL droplet volumes in three different locations for each condition. One Touch Grabber and Image J were used to calculate the obtained contact angles.

2.7. Cell viability and adhesion assays. Scaffolds were sterilized with ethanol for 30 minutes and under UV light (405nm) for 1 hour. MG-63 osteosarcoma and MC3T3-E1 preosteoblast cells were cultured on the sterilized scaffolds in MEM alpha, 10% FBS and 1% penicillin/streptomycin for up to 7 days before cell viability and adhesion assays. Cell viability and proliferation were analyzed with the MTT assay. At different time points during culture, 100 µL of culture medium containing 0.05 $mg.mL^{-1}$ of MTT solution was added to the cultures for 3h. MTT reduction by living cells leads to the production of purple-colored

formazan crystals that were solubilized by addition of 100 µL of DMSO (BDH Prolab 23486.297). The absorbance of the formazan solution was recorded at 560 nm using a Multiskan plate reader (Thermos, USA). For the adhesion assay, MG-63 cells and MC3T3-E1 preosteoblast were fixed in 4% formaldehyde (500 µL/well) at room temperature for 20 minutes. Fixed cells were washed with PBS, permeabilized with PBS/0.1% Triton X 100 (Sigma) for 15 minutes, and incubated with PBS/1% BSA solution for 3 hours. Then, the cell cytoskeleton was stained with an anti-actin antibody at 4°C overnight. After two washes with PBS/0.05% Tween 20, an Alexa-conjugated anti-mouse IgG secondary antibody was added with Hoechst 33342, to stain the nuclei, at room temperature for 1 hour. Samples were mounted in Mowiol and fluorescent images were recorded using a fluorescent microscope (DM6000 Leica). Cells attachment and morphology on the scaffolds were recorded using SEM. MG-63 Cells were cultured for 48 hours days on the scaffolds and fixed using 2.5% of Glutaraldehyde for 30 min. Scaffolds were washed using serial concentrations of ethanol (30%, 50%, 70%, 90%, and absolute ethanol). The scaffolds were then treated with 1 mL of hexamethyldisilazane to dry the sample. Scaffolds were finally coated with platinum using a Mini Sputter Coater before to be observed with SEM.

2.8. Mineralization assay. MG-63 cells were plated in Petri dishes on the scaffolds and grown until confluence (day 0). Then, medium was switched to differentiation medium supplemented with ascorbic acid (50 $mg.ml^{-1}$), ß-glycerophosphate (5 mM) and dexamethasone (10^{-8} M), and refreshed every 48 hours. Formation of mineralized nodules was monitored at day 0, 14 and 21 by Alizarin Red-S staining. Briefly, cells were rinsed twice with PBS followed by fixation in 4% formaldehyde at room temperature for 20 minutes. Then, cells were rinsed twice with PBS (pH 4.2) and stained with 40 mM Alizarin Red-S (pH 4.2) at room temperature for 20 minutes, and extensively rinsed with water. For

quantification, the staining was eluted with 10% (wt/vol) cetylpyridinium chloride, and the supernatant absorbance was measured at 540 nm using a microplate reader (Bio-Rad). Differences between groups were assessed with the Student's *t*-test and were considered significant at *$p<0.05$ and **$p<0.005$.

3. RESULTS AND DISCUSSION.

3.1. Structural and chemical characterization of the scaffolds. To reinforce PLA, EBN fillers were added to the polymer matrix at 0.1% wt. The composite was extruded *via* a single screw extruder and put in shape using a FDM system. PLA before extrusion is denoted as PLA-film (see Figure 1 for a schematic representation of the working plan).

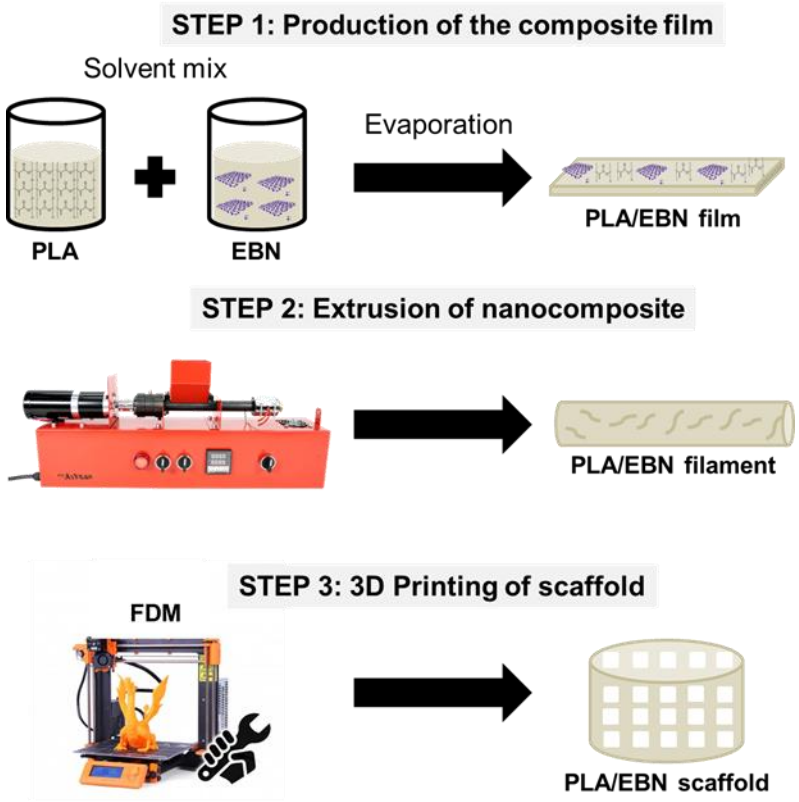

Figure 1. Schematic representation of the different steps leading to scaffold generation (production of the composite film, extrusion of the nanocomposite and 3D printing)

In a first step, we characterized the chemical and structural properties of the nanocomposites. BN Raman spectrum showed a characteristic band at 1390 cm^{-1} that corresponded to the E2g mode (Figure 2a). PLA-film spectrum showed the characteristic bands at 1127, 1294, 1447 and 1764 cm^{-1} (asterisks in Figure 2a). In the PLA/EBN spectrum, the morphology and intensity of the characteristic Raman band at 1390 cm^{-1} changed compared with the PLA spectrum (arrows in Figure 2a). This change confirmed EBN incorporation in the polymer matrix.

To understand PLA organization and BN interactions with the polymer matrix during the nanocomposite fabrication, FTIR spectra were recorded (Figure 2b). The two major EBN peaks observed at 1271 and 763 cm^{-1} were assigned to B−N stretching and out-of-plane B−N bending in the hexagonal rings, respectively. A slight difference between the peaks at 1231 cm^{-1} of pure PLA and PLA/EBN was observed (arrows). This could be due to EBN incorporation, but cannot be confirmed because the absorbance of the PLA peaks was greater than that of EBN. In addition, the EBN peaks were in the same range as those of PLA and thus were covered by them.

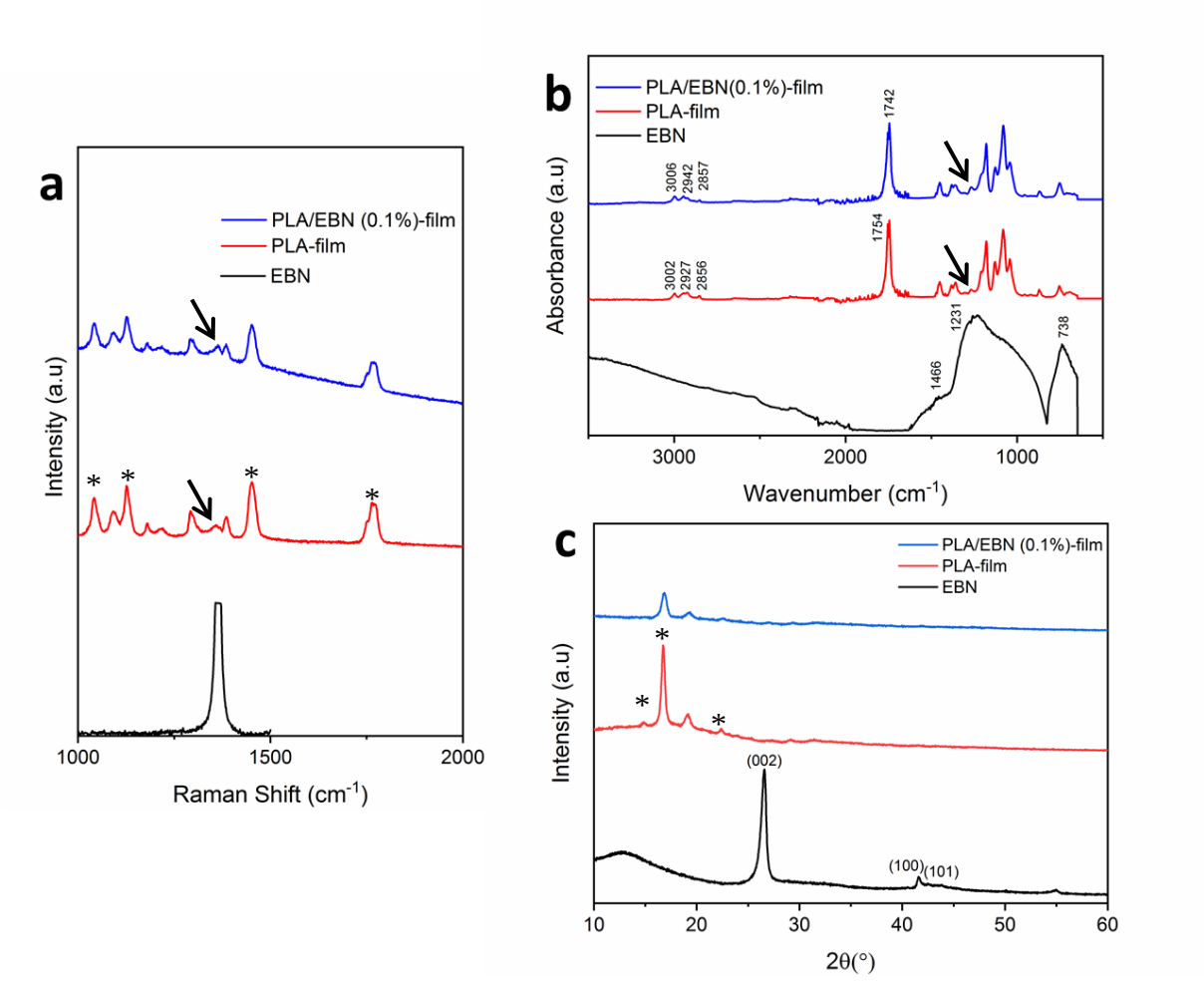

Figure 2. Chemical and structural properties of the nanocomposites: (a) Raman spectroscopy, (b) FTIR spectra, and (c) XRD diffractograms of exfoliated boron nitride (EBN), PLA-film, and PLA/EBN nanocomposites.

The XRD patterns of the scaffolds are shown in Figure 2c. PLA-film showed four characteristics peaks at 2θ = 15, 17, 19 and 23° that described the alpha form of PLA[49].

Concerning the PLA/EBN composites before extrusion, the characteristic PLA peaks were maintained, although they were broader, possibly due to micro-stresses induced by BN in the polymer matrix. The peaks at 2θ = 26°, 41.5° and 43.7° corresponding to the (002), (100), and (101) planes of BN[3] did no longer appear, showing the good BN exfoliation in the PLA matrix.

3.2. Thermal analysis of the PLA/EBN scaffolds.

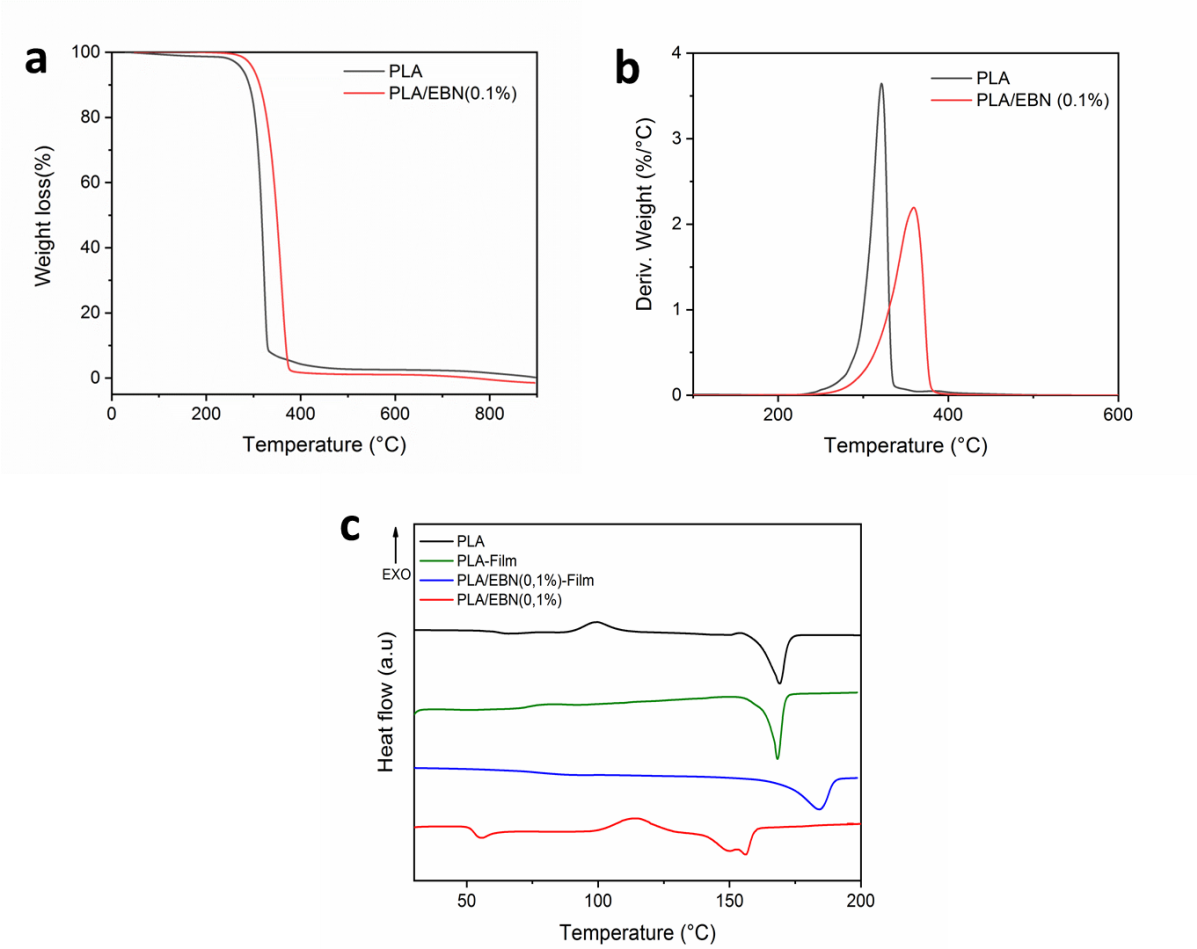

Figure 3. Thermal properties of nanocomposite materials: (a) TGA, and (b) derivative TGA curves of 3D printed PLA/EBN nanocomposites; (c) representative DSC graphs showing Tg, Tcc and Tm of PLA and PLA/EBN nanocomposites.

BN influence on PLA thermal stability was monitored by TGA analysis (Figure 3a). For PLA, the 1% weight loss observed below 200°C was due to the adsorbed water. The second major weight loss, observed between 300 and 400°C, showed the degradation of the PLA polymer

with a maximum loss at 298°C. The third major weight loss, observed from ~410°C, was due to the thermochemical decomposition of the remaining organic content. Concerning PLA/EBN, the first weight loss was observed at 225°C. The major decrease that corresponded to the degradation of the polymer composite was observed at 359°C, and the last degradation step was observed from 400°C with a weight loss of 3%.

Moreover the peak of maximum degradation temperature shifted from 298°C for PLA to 359°C for the nanocomposites with 0.1% of BN, as shown in the derivative weight curves (Figure 3b). The two curves showed little difference; however, this mass loss corresponding to the cleavage of the polymer chains started with an offset of 62°C for PLA/BN compared with pure PLA. This may be due to the relatively small amount of BN particles present in the sample, and to a low thermal barrier effect caused by BN. BN particles are expected to retard degradation, and randomly protect a few inner layers of polymer. BN trapped the degradation products inside the polymer by dissipating the heat in the planar direction. When the heat energy is absorbed, the thermal equilibrium is reached[50]. Samples exhibited strong interaction with BN, which resulted in the high thermal stability of the composites.

EBN influence on PLA crystallinity and on *Tg*, *Tcc* and *Tm* were evaluated by DSC analysis (Figure 3c). Enthalpy of fusion, glass transition and melting point were measured and are summarized in Table 1, together with the calculated crystallinity. The *Tg* and *Tm* of PLA were 59°C and 168°C before (PLA-film) and 61°C and 169°C after extrusion, respectively. This indicated that the extrusion process did not affect PLA thermal properties. After extrusion, PLA showed a cold crystallization peak at 100°C that was not present in the PLA-film before extrusion (Figure 3c), as reported in a previous study[51].

Table 1. Temperatures, enthalpies of different thermal transitions and crystallinity of PLA and PLA/EBN

Samples	Tg (°C)	Tm (°C)	ΔHf (J/g)	ΔHcf (J/g)	χ (%)
PLA-film	59±0.7	168±0.4	30±1	-	32±1
PLA	61±1.4	169±0,1	30±0,1	10±0,2	21±0,3
PLA/EBN-film	59±0.8	155±1,5	18±1,6	-	19±1,3
PLA/EBN	53±2	156±0,2	22±3,1	17±5	5±2

In line with these observations, PLA crystallinity was lower after (21%) than before (32%) extrusion, and this change could have been caused by the extrusion process[52]. For PLA reinforced with 0.1% BN before extrusion, the *Tg* was 59°C, and decreased to 53°C after extrusion. This was followed by an exothermic cold crystallization peak at 110°C (Figure 3c). Addition of EBN significantly decreased the PLA *Tm* from 169°C to 156°C after extrusion, and this was associated with the appearance of a double melting peak at 156 °C (Figure 3c). This suggests the presence of two sizes of crystallites that could have been induced by BN charges in the polymer matrix.

After extrusion, EBN addition decreased PLA crystallinity from 21% to 5%. This lower crystallinity of the PLA/EBN scaffold could be due to the number of interacting sites between the polymer matrix and the filler that might reduce the PLA chain mobility. Additionally, EBN aggregates may have physically disturbed the polymer crystallization. Finally, thermal analysis by TGA and DSC showed that EBN presence in the polymer matrix did not affect filament extrusion. The 3D printing conditions also were not influenced by EBN addition. However, EBN increased the thermal stability of the nanocomposite scaffolds.

3**.3. Mechanical properties of the 3D printed nanocomposites.** Composites used for bone tissue engineering applications must withstand high loads. Therefore, the mechanical properties of PLA and PLA/EBN nanocomposites were analyzed using dog bone shaped samples (Figure S1). For bone engineering, the elastic region is a very important parameter

and therefore, it was important to determine the influence of EBN addition on PLA elastic modulus. The Young's modulus of PLA increased with EBN from 2 to 2.2 GPa (not statistically significant) (Figure 4). Similarly, tensile stress at break and Poisson's ratio were not significantly different in PLA and PLA/EBN samples. This demonstrates that EBN addition did not affect the mechanical properties of the PLA scaffold, and that EBN can be used as a filler to improve the bioactivity of PLA scaffolds without effects on their mechanical properties.

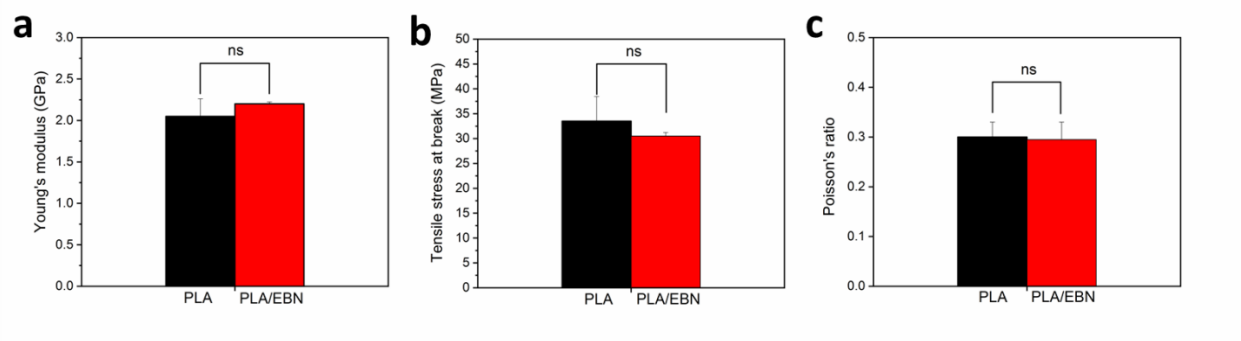

Figure 4. Mechanical properties of the scaffolds: (a) Young's modulus, (b) Tensile stress at break, and (c) Poisson's ratio of PLA and PLA/EBN nanocomposites (ns= not significant).

3.4. Morphological analysis of PLA/EBN scaffolds. To facilitate bone regeneration, scaffolds with a porous interconnected network and pore size between 300 µm and 500 µm were generated. SEM was used to analyze EBN effect on the morphology and pore size of the 3D printed PLA/EBN scaffolds. SEM micrographs revealed the scaffold porous morphology (Figures 5a and b). The pores size of PLA scaffolds was 405 µm (±20) with a wall width of 380µm (±65), which is crucial for osteoblast cell infiltration and good mineralization[53–55]. Indeed, the influence of pores size on cell proliferation and migration was well demonstrated[55,56]. The shift of pores sizes with EBN addition might have an impact on the cells proliferation on the scaffolds. EBN addition to the PLA resulted in a modification of the

composite filament. This change led to an increase in pore size during printing. The reduction of the walls separating the pores led to pore enlargement in the scaffold.

The 3D topography images allowed comparing the surfaces of the PLA and PLA/EBN composite scaffolds (Figures 5c and d). The scaffold surface was modified upon EBN incorporation in the polymer matrix. Scaffolds with EBN incorporation presented higher positive values of Sa than PLA scaffolds, due to the filler presence at the surface and fine dispersions in the polymer matrix (Table 2).

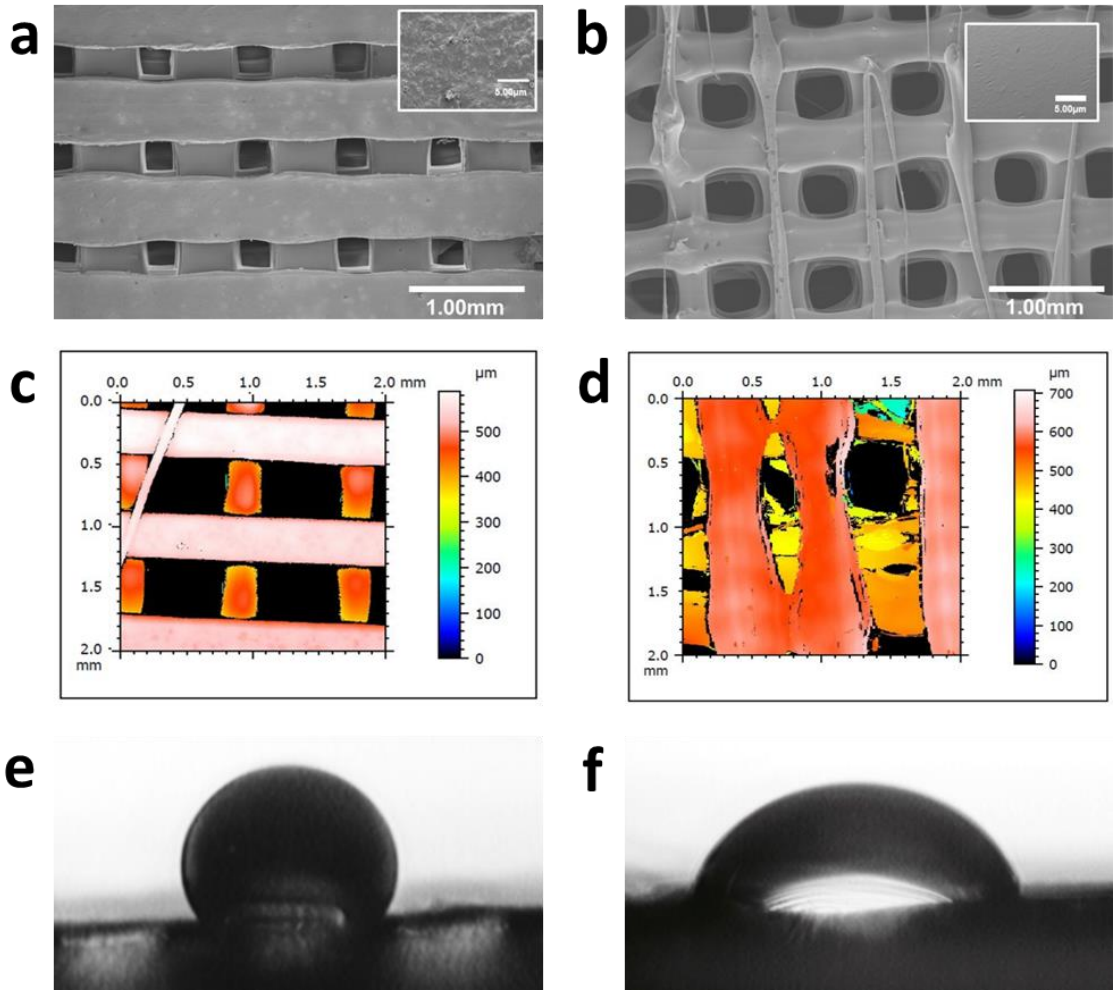

Figure 5. Scanning electron micrographs of FDM-based 3D printed PLA and PLA/EBN scaffolds: Top view of the architecture of 3D printed (a) PLA and (b) PLA/EBN scaffolds; inset, zoom showing the surface. Topography of the scaffolds: Representative 3D images of the surface roughness of PLA (c) and PLA/EBN (d) scaffolds. Images showing the contact angle of water on: (e) PLA and (f) PLA/EBN scaffolds.

In bone tissue engineering, the surface chemistry of biomedical devices is very important. It influences the material hydrophilicity and is required for cell attachment to the scaffold surface to proliferate and differentiate for bone regeneration[57]. The measurements of water contact angles (Figures 5e and f) showed a significant reduction of the values ($p < 0.00005$) for PLA/EBN scaffolds compared with PLA (Table 2). In summary, EBN addition significantly improved the PLA scaffold hydrophilic character.

Table 2. Roughness parameters and contact angles of PLA and PLA/EBN scaffolds with H_2O: Sa – arithmetical mean height of the surface.

Samples	Pore size (µm)	Wall width (µm)	Sa (µm)	Contact angles (°)
PLA	405 ± 20	380 ± 65	5.8 ± 1.5	118 ± 6
PLA/EBN	500 ± 80	350 ± 25	9.3 ± 2.7	80 ± 13

3.5. Biological studies. The biocompatibility of 3D printed PLA/EBN scaffolds was investigated using MG-63 osteosarcoma and MC3T3-E1 preosteoblast cells that display osteogenic potential[58]. EBN effect on cell viability, attachment and proliferation was analyzed and compared with the results obtained for cells grown with PLA scaffolds and without scaffolds (control). The presence of EBN (0.1%) in the scaffold did not affect viability (MTT assay) after 4 or 7 days of culture (Figure 6a and 6b). This suggests that 3D printed PLA/EBN scaffolds do not release any toxic fragment and that direct contact of cells with EBN is possible without damage.

Interestingly, previous research using conducting polymers (particularly polypyrrole (Ppy)) reported no significant toxicity towards mouse peritoneum cells, whereas some toxicity of Ppy nanoparticles was detected towards bone marrow-derived stem cells[59,60]. The toxicity towards stem cells was dose-dependent and, at lower concentrations, PPy did not show any toxicity towards other cell types including primary mouse embryonic fibroblasts (MEF), mouse hepatoma cell line (MH-22A), and human T lymphocyte Jurkat cells[61].

Cell attachment and proliferation on the scaffolds was monitored by staining the cytoskeleton with an anti-actin antibody and nuclei with Hoechst 333342 at day 1 and 4. As shown in Figure 6c, EBN incorporation increased MG-63 cell attachment monitored after 1 day of culture. This was confirmed using the MTT assay at day 1 (Figure 6d) and was also observed with MC3T3 cells (data not shown). Similarly, quantification of cell proliferation at days 4 and 7 confirmed that the PLA/EBN scaffolds promoted cell proliferation at higher levels than the PLA scaffold (Figure 6d). SEM analysis performed after 7 days of culture until maximum confluence (Figure 6c) confirmed cell proliferation on the PLA and PLA/EBN scaffolds with cells appearing less flattened on the PLA/EBN scaffold. Altogether, these data indicated that EBN incorporation in the PLA scaffolds increased their cytocompatibility.

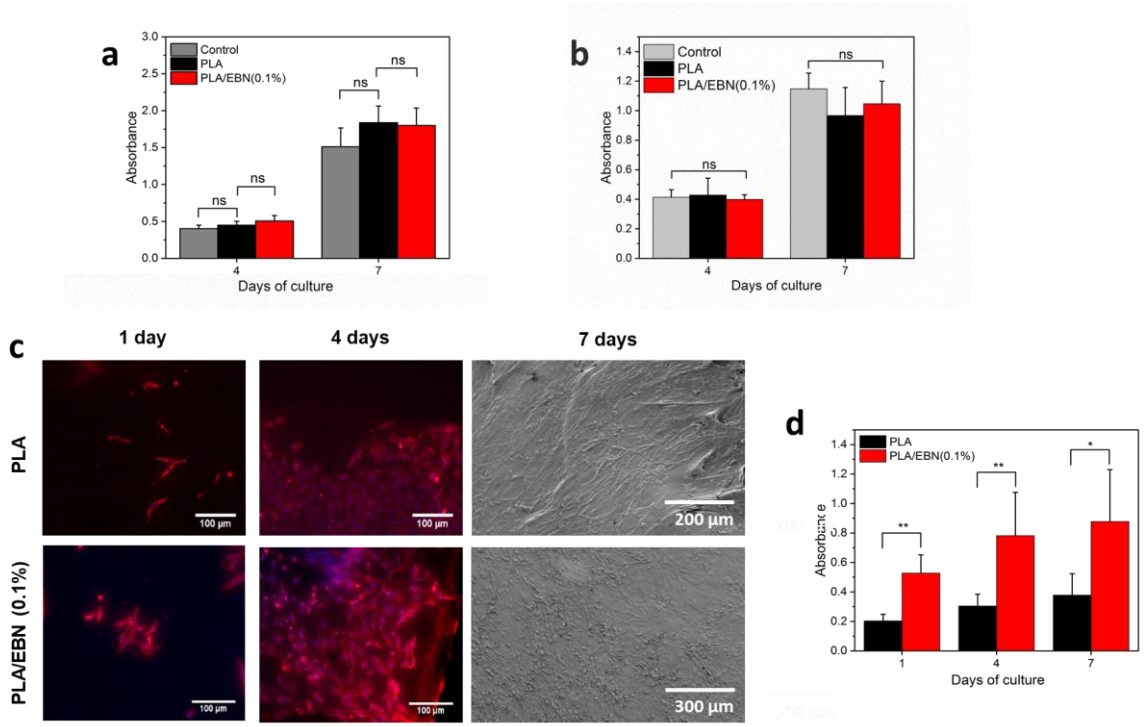

Figure 6. Cell viability of MG-63 cells (a) and MC3T3-E1 cells (b) grown on PLA and PLA/EBN scaffolds assessed with the MTT at day 4 and 7 (ns = not significant), (c) MG-63 cell attachment on PLA nanocomposites was analyzed by immunofluorescence staining of actin (red), DNA staining (blue) and SEM at the indicated time points and (d) cell proliferation of MG-63 (MTT assay) (ns = not significant, *p<0.05, **p<0.005).

Finally, mineralization (i.e., calcium deposition on scaffolds by MG-63 cells) was determined by colorimetric quantification after Alizarin Red-S staining at day 1, 14 and 21 of culture (Figure 7). A significantly higher calcium deposition was observed at day 21 in cultures with PLA/EBN scaffolds compared with PLA scaffolds, demonstrating the good mineralization on scaffolds. This effect could be linked to EBN interaction with the matrix and the modification of surface states or pore size upon EBN incorporation. These results demonstrate that EBN is biocompatible and shows good bioactivity by enhancing MG-63 cell mineralization activity.

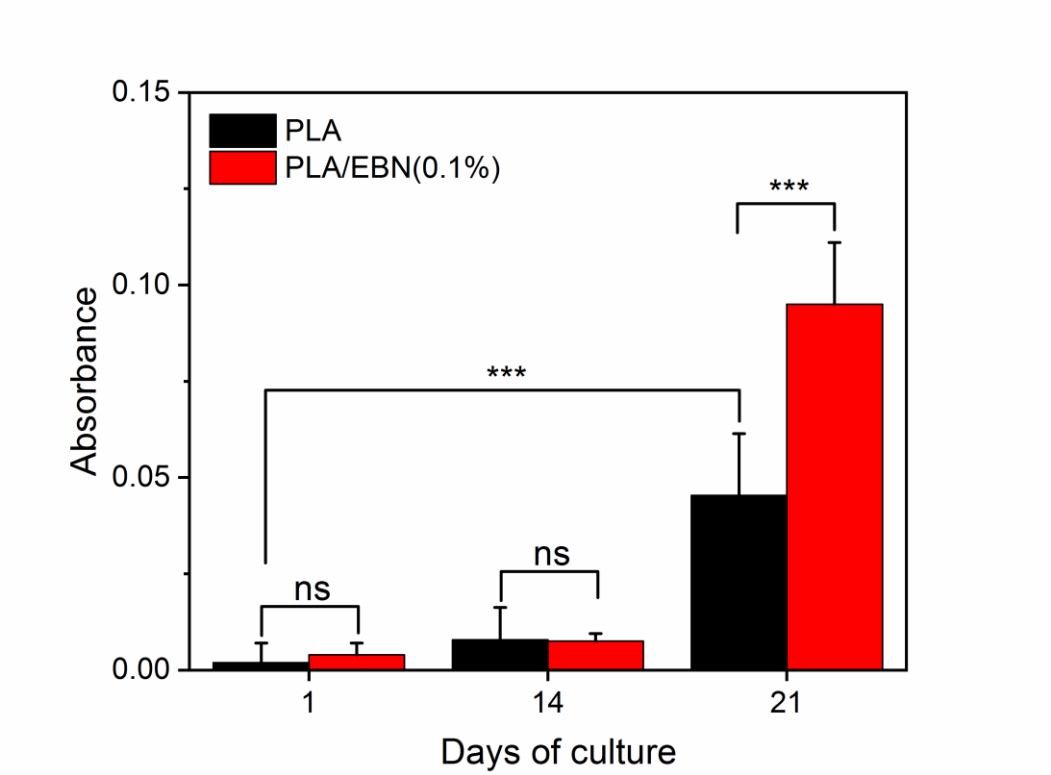

Figure 7. Mineralization evaluated by Alizarin Red-S staining of MG-63 cells cultured on PLA and PLA/EBN nanocomposite scaffolds at the indicated time points after switching to differentiation medium (ns = not significant, *p<0.05).

4. CONCLUSIONS.

This study shows that it is possible to fabricate PLA/EBN nanocomposites with controlled morphology and a network of interconnected pores around 500 μm using FDM-assisted 3D printing. Altogether, our results demonstrated that EBN incorporation 1) increased the polymer surface roughness and decreased its hydrophobicity, 2) enhanced the polymer

thermal stability, 3) decreased the polymer crystallinity, 4) did not affect the scaffold mechanical properties, and 5) promoted bone cell attachment, proliferation and differentiation. Our data clearly indicate that PLA reinforcement with 0.1% EBN could represent a good strategy to obtain 3D printed scaffolds with attractive bioactivity for a potential application in bone tissue engineering.

Acknowledgments:

We acknowledge the financial support from Indo-French Centre for the promotion of advanced research-Cefipra (Project 5608-1), from CNRS (Project “Osez l'Interdisciplinarité: TraitCancer”) and from University of Montpellier (MUSE “3DTraitCancer”). The authors thank Hélène Garay (Centre des Matériaux des Mines d’Alès, IMT mines d’Alès, France) for assistance in topography characterizations. We kindly thank Olivier Peyruchaud (Lyos, Inserm UMR 1033, Lyon, France) for the gift of MC3T3-E1 cells.

5. REFERENCES.

1. Tang, D. *et al.* Biofabrication of bone tissue: Approaches, challenges and translation for bone regeneration. *Biomaterials* **83,** 363–382 (2016).
2. Aro, H. T. & Aho, A. J. Clinical use of bone allografts. *Ann. Med.* **25,** 403–412 (1993).
3. Rezwan, K., Chen, Q. Z., Blaker, J. J. & Boccaccini, A. R. Biodegradable and bioactive porous polymer/inorganic composite scaffolds for bone tissue engineering. *Biomaterials* **27,** 3413–3431 (2006).
4. Bose, S., Roy, M. & Bandyopadhyay, A. Recent advances in bone tissue engineering scaffolds. *Trends Biotechnol.* **30,** 546–554 (2012).
5. Teixeira, A. I., Abrams, G. A., Bertics, P. J., Murphy, C. J. & Nealey, P. F. Epithelial contact guidance on well-defined micro- and nanostructured substrates. *J. Cell Sci.* **116,** 1881–1892 (2003).
6. Wang, Y. *et al.* The predominant role of collagen in the nucleation, growth, structure and orientation of bone apatite. *Nat. Mater.* **11,** 724–733 (2012).
7. Engler, A. J., Sen, S., Sweeney, H. L. & Discher, D. E. Matrix Elasticity Directs Stem Cell Lineage Specification. *Cell* **126,** 677–689 (2006).
8. Nagarajan, S. *et al.* Design of Boron Nitride/Gelatin Electrospun Nanofibers for Bone Tissue Engineering. *ACS Appl. Mater. Interfaces* **9,** 33695–33706 (2017).
9. Temple, J. P. *et al.* Engineering anatomically shaped vascularized bone grafts with hASCs and 3D-printed PCL scaffolds. *J. Biomed. Mater. Res. - Part A* **102,** 4317–4325 (2014).
10. Lasprilla, A. J. R., Martinez, G. A. R., Lunelli, B. H., Jardini, A. L. & Maciel Filho, R. Poly-lactic acid synthesis for application in biomedical devices—A review. *Biotechnol. Adv.* **30,** 321–328 (2012).
11. Muller, J., González-Martínez, C. & Chiralt, A. Combination Of Poly(lactic) acid and starch for biodegradable food packaging. *Materials (Basel).* **10,** 1–22 (2017).
12. Babu, R. P., O'Connor, K. & Seeram, R. Current progress on bio-based polymers and their future trends. *Prog. Biomater.* **2,** 8 (2013).
13. Cutright, D. E. & Hunsuck, E. E. Tissue reaction to the biodegradable polylactic acid suture. *Oral Surgery, Oral Med. Oral Pathol.* **31,** 134–139 (1971).
14. Bos, R. R. M. *et al.* Degradation of and tissue reaction to biodegradable poly (L-lactide) for use as internal fixation of fractures: a study in rats. *Biomaterials* **12,** 32–36 (1991).
15. Hamad, K., Kaseem, M., Yang, H. W., Deri, F. & Ko, Y. G. Properties and medical applications of polylactic acid: A review. *Express Polym. Lett.* **9,** (2015).
16. Kumar, A., Rao, T. V., Chowdhury, S. R. & Reddy, S. V. S. R. Compatibility confirmation and refinement of thermal and mechanical properties of poly (lactic acid)/poly (ethylene-co-glycidyl methacrylate) blend reinforced by hexagonal boron nitride. *React. Funct. Polym.* **117,** 1–9 (2017).
17. Ciofani, G., Raffa, V., Menciassi, A. & Cuschieri, A. Boron nitride nanotubes: an innovative tool for nanomedicine. *Nano Today* **4,** 8–10 (2009).
18. Golberg, D. *et al.* Boron nitride nanotubes and nanosheets. *ACS Nano* (2010). doi:10.1021/nn1006495
19. Biscarat, J., Bechelany, M., Pochat-Bohatier, C. & Miele, P. Graphene-like BN/gelatin nanobiocomposites for gas barrier applications. *Nanoscale* **7,** 613–618 (2015).
20. Lahiri, D. *et al.* Boron nitride nanotube reinforced polylactide–polycaprolactone copolymer composite: mechanical properties and cytocompatibility with osteoblasts and macrophages in vitro. *Acta Biomater.* **6,** 3524–3533 (2010).
21. Nagarajan, S. *et al.* Design of graphene-like boron nitride/gelatin electro spun nanofibers as new bio nanocomposite material for tissue engineering.
22. Ciofani, G., Raffa, V., Menciassi, A. & Cuschieri, A. Cytocompatibility, interactions, and uptake of polyethyleneimine-coated boron nitride nanotubes by living cells: Confirmation of their potential for biomedical applications. *Biotechnol. Bioeng.* **101,** 850–858 (2008).
23. I. Scorei, R. & Popa, R. Boron-Containing Compounds as Preventive and Chemotherapeutic Agents for Cancer. *Anticancer. Agents Med. Chem.* **10,** 346–351 (2012).
24. Weng, Q. *et al.* Highly water-soluble, porous, and biocompatible boron nitrides for anticancer drug delivery. *ACS Nano* **8,** 6123–6130 (2014).
25. Li, X. *et al.* Boron nitride nanotube-enhanced osteogenic differentiation of mesenchymal stem cells. *J. Biomed. Mater. Res. - Part B Appl. Biomater.* (2016). doi:10.1002/jbm.b.33391
26. Salvetti, A. *et al.* In vivo biocompatibility of boron nitride nanotubes: Effects on stem cell biology and tissue regeneration in planarians. *Nanomedicine* (2015). doi:10.2217/nnm.15.46
27. Liao, C. *et al.* Fabrication of porous biodegradable polymer scaffolds using a solvent merging/particulate leaching method. *J. Biomed. Mater. Res. An Off. J. Soc. Biomater. Japanese Soc. Biomater. Aust. Soc. Biomater. Korean Soc. Biomater.* **59,** 676–681 (2002).
28. Sultana, N. & Wang, M. PHBV/PLLA-based composite scaffolds fabricated using an emulsion freezing/freeze-drying technique for bone tissue engineering: surface modification and in vitro biological

evaluation. *Biofabrication* **4,** 15003 (2012).
29. Huang, Y. X., Ren, J., Chen, C., Ren, T. B. & Zhou, X. Y. Preparation and properties of poly (lactide-co-glycolide)(PLGA)/nano-hydroxyapatite (NHA) scaffolds by thermally induced phase separation and rabbit MSCs culture on scaffolds. *J. Biomater. Appl.* **22,** 409–432 (2008).
30. Nagarajan, S. *et al.* Design of graphene oxide/gelatin electrospun nanocomposite fibers for tissue engineering applications. *RSC Adv.* **6,** 109150–109156 (2016).
31. Murphy, S. V & Atala, A. 3D bioprinting of tissues and organs. *Nat. Biotechnol.* **32,** 773 (2014).
32. Chia, H. N. & Wu, B. M. Recent advances in 3D printing of biomaterials. *J. Biol. Eng.* **9,** 4 (2015).
33. Gauvin, R. *et al.* Microfabrication of complex porous tissue engineering scaffolds using 3D projection stereolithography. *Biomaterials* **33,** 3824–3834 (2012).
34. Luo, Y., Lode, A., Akkineni, A. R. & Gelinsky, M. Concentrated gelatin/alginate composites for fabrication of predesigned scaffolds with a favorable cell response by 3D plotting. *RSC Adv.* **5,** 43480–43488 (2015).
35. Williams, J. M. *et al.* Bone tissue engineering using polycaprolactone scaffolds fabricated via selective laser sintering. *Biomaterials* **26,** 4817–4827 (2005).
36. Murphy, S. V. & Atala, A. 3D bioprinting of tissues and organs. *Nat. Biotechnol.* **32,** 773–785 (2014).
37. Serra, T., Planell, J. A. & Navarro, M. High-resolution PLA-based composite scaffolds via 3-D printing technology. *Acta Biomater.* **9,** 5521–5530 (2013).
38. Senatov, F. S. *et al.* Mechanical properties and shape memory effect of 3D-printed PLA-based porous scaffolds. *J. Mech. Behav. Biomed. Mater.* **57,** 139–148 (2016).
39. Gómez, S., Vlad, M. D., López, J. & Fernández, E. Design and properties of 3D scaffolds for bone tissue engineering. *Acta Biomater.* **42,** 341–350 (2016).
40. Rogina, A. *et al.* Macroporous poly(lactic acid) construct supporting the osteoinductive porous chitosan-based hydrogel for bone tissue engineering. *Polymer* **98,** 172–181 (2016).
41. Rosenzweig, D. H., Carelli, E., Steffen, T., Jarzem, P. & Haglund, L. 3D-printed ABS and PLA scaffolds for cartilage and nucleus pulposustissue regeneration. *Int. J. Mol. Sci.* **16,** 15118–15135 (2015).
42. Liu, J., Li, W., Guo, Y., Zhang, H. & Zhang, Z. Improved thermal conductivity of thermoplastic polyurethane via aligned boron nitride platelets assisted by 3D printing. *Compos. Part A Appl. Sci. Manuf.* **120,** 140–146 (2019).
43. Quill, T. J. *et al.* Thermal and mechanical properties of 3D printed boron nitride – ABS composites. *Appl. Compos. Mater.* **25,** 1205–1217 (2018).
44. Bustillos, J., Montero-Zambrano, D., Loganathan, A., Boesl, B. & Agarwal, A. Stereolithography-based 3D printed photosensitive polymer/boron nitride nanoplatelets composites. *Polym. Compos.* **40,** 379–388 (2019).
45. Guiney, L. M. *et al.* Three-Dimensional Printing of Cytocompatible, Thermally Conductive Hexagonal Boron Nitride Nanocomposites. *Nano Lett.* **18,** 3488–3493 (2018).
46. Vu, T.-L. & Barés, J. Soft grain compression: beyond the jamming point. (2019).
47. Vu, T. L., Barés, J., Mora, S. & Nezamabadi, S. Deformation Field in Diametrically Loaded Soft Cylinders. *Exp. Mech.* (2019). doi:10.1007/s11340-019-00477-4
48. Lee, S. J. *et al.* Vascular endothelial growth factor immobilized on mussel-inspired three-dimensional bilayered scaffold for artificial vascular graft application: In vitro and in vivo evaluations. *J. Colloid Interface Sci.* **537,** 333–344 (2019).
49. Campos, J. M., Ferraria, A. M., Botelho Do Rego, A. M., Ribeiro, M. R. & Barros-Timmons, A. Studies on PLA grafting onto graphene oxide and its effect on the ensuing composite films. *Materials Chemistry and Physics* **166,** 122–132 (2015).
50. Barkoula, N.-M., Alcock, B., Cabrera, N. O. & Peijs, T. Fatigue properties of highly oriented polypropylene tapes and all-polypropylene composites. *Polym. Polym. Compos.* **16,** 101–113 (2008).
51. Huda, M. S., Yasui, M., Mohri, N., Fujimura, T. & Kimura, Y. Dynamic mechanical properties of solution-cast poly(L-lactide) films. *Mater. Sci. Eng. A* **333,** 98–105 (2002).
52. Ravi, P., Shiakolas, P. S. & Welch, T. R. Poly-L-lactic acid: Pellets to fiber to fused filament fabricated scaffolds, and scaffold weight loss study. *Addit. Manuf.* **16,** 167–176 (2017).
53. Di Luca, A. *et al.* Gradients in pore size enhance the osteogenic differentiation of human mesenchymal stromal cells in three-dimensional scaffolds. *Sci. Rep.* **6,** 1–13 (2016).
54. Matsiko, A., Gleeson, J. P. & O'Brien, F. J. Scaffold Mean Pore Size Influences Mesenchymal Stem Cell Chondrogenic Differentiation and Matrix Deposition. *Tissue Eng. Part A* **21,** 486–497 (2014).
55. Bružauskaitė, I., Bironaitė, D., Bagdonas, E. & Bernotienė, E. Scaffolds and cells for tissue regeneration: different scaffold pore sizes—different cell effects. *Cytotechnology* **68,** 355–369 (2016).
56. Karageorgiou, V. & Kaplan, D. Porosity of 3D biomaterial scaffolds and osteogenesis. *Biomaterials* **26,** 5474–5491 (2005).
57. Mitra, J., Tripathi, G., Sharma, A. & Basu, B. Scaffolds for bone tissue engineering: Role of surface

patterning on osteoblast response. *RSC Advances* (2013). doi:10.1039/c3ra23315d
58. Czekanska, E. M., Stoddart, M. J., Ralphs, J. R., Richards, R. G. & Hayes, J. S. A phenotypic comparison of osteoblast cell lines versus human primary osteoblasts for biomaterials testing. *J. Biomed. Mater. Res. Part A* **102,** 2636–2643 (2014).
59. Ramanaviciene, A., Kausaite, A., Tautkus, S. & Ramanavicius, A. Biocompatibility of polypyrrole particles: an in-vivo study in mice. *J. Pharm. Pharmacol.* **59,** 311–315 (2007).
60. Vaitkuviene, A. *et al.* Evaluation of cytotoxicity of polypyrrole nanoparticles synthesized by oxidative polymerization. *J. Hazard. Mater.* **250–251,** 167–174 (2013).
61. Vaitkuviene, A. *et al.* Some biocompatibility aspects of conducting polymer polypyrrole evaluated with bone marrow-derived stem cells. *Colloids Surfaces A Physicochem. Eng. Asp.* **442,** 152–156 (2014).